

Transverse-Field Ising Dynamics in a Rydberg-Dressed Atomic Gas

V. Borish,¹ O. Marković,² J. A. Hines,¹ S. V. Rajagopal,² and M. Schleier-Smith²

¹*Department of Applied Physics, Stanford University, Stanford, California 94305, USA*

²*Department of Physics, Stanford University, Stanford, California 94305, USA*

(Dated: December 28, 2023)

We report on the realization of long-range Ising interactions in a cold gas of cesium atoms by Rydberg dressing. The interactions are enhanced by coupling to Rydberg states in the vicinity of a Förster resonance. We characterize the interactions by measuring the mean-field shift of the clock transition via Ramsey spectroscopy, observing one-axis twisting dynamics. We furthermore emulate a transverse-field Ising model by periodic application of a microwave field and detect dynamical signatures of the paramagnetic-ferromagnetic phase transition. Our results highlight the power of optical addressing for achieving local and dynamical control of interactions, enabling prospects ranging from investigating Floquet quantum criticality to producing tunable-range spin squeezing.

Optically controlled interactions among cold atoms are a powerful tool for fundamental studies of quantum many-body dynamics [1–17] and for engineering entangled states [18–25]. Tailoring interactions with light theoretically allows for accessing non-equilibrium phases of matter [14, 26–28], studying inhomogeneous quantum phase transitions [29], implementing quantum optimization algorithms [30, 31], and enhancing quantum sensors [32–34]. Demonstrated approaches to optical control include coupling atoms to Rydberg states [1–7, 18–22], optical resonators [8–10, 23, 24], or molecular bound states [11, 12, 35–38]. Among these approaches, Rydberg excitation is notable for producing strong interactions on the few-micron scale—a typical interatomic spacing in a laser-cooled gas or optical tweezer array [4–6].

An alternative to direct excitation is Rydberg dressing, i.e., inducing interactions among ground-state atoms by coupling to Rydberg states with an off-resonant laser field [15–17, 25]. Rydberg dressing offers the benefit of dynamical control over the strength and form of interactions, as well as a long coherence time once the light is switched off. Maximizing the coherence of the interactions themselves has been the focus of several recent experiments [39–41]. While efforts at dressing in dense 3D lattices have suffered from runaway loss and dephasing [40–42], Rydberg-dressed interactions have been successfully applied to entangle atoms in optical tweezers [22] and to study coherent many-body spin dynamics in one- and two-dimensional atom arrays [2, 3].

The simplest form of interaction realizable by Rydberg dressing is an Ising interaction, where the Ising spins are encoded in two hyperfine ground states. However, applications in quantum simulation [14], quantum optimization [30, 31], and quantum state engineering [34] additionally require a transverse field, which allows quantum correlations to spread. Transverse-field Ising models can undergo a phase transition from paramagnetic to ferromagnetic, which has been studied in mean-field dynamics of Bose-Einstein condensates [43] and in trapped-ion spin chains [44, 45]. Time-dependent variants of the model furthermore yield a rich diagram of Floquet

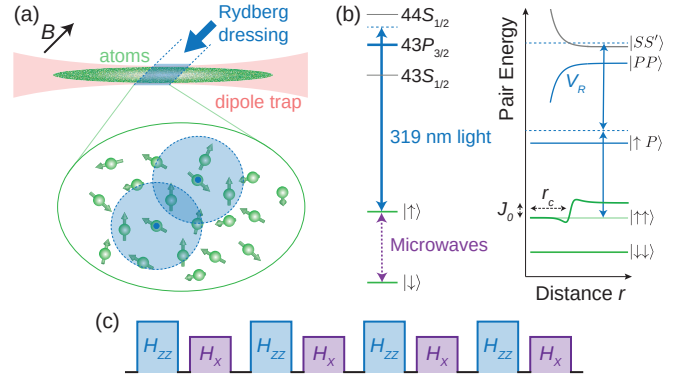


FIG. 1. Experimental setup and Rydberg dressing scheme. (a) A cloud of cesium atoms is held in an optical dipole trap and locally illuminated with 319 nm light to generate Ising interactions of characteristic range r_c and strength J_0 . (b) Energy level diagrams for a single atom (left) and for a pair of atoms (right). (c) Alternating between interactions (H_{zz}) and microwave rotations (H_x) produces an effective transverse-field Ising model.

phases, including time crystals [26, 46] and predicted Floquet symmetry-protected topological phases [14, 26, 27].

In this Letter, we report on the realization of a transverse-field Ising model in a dilute gas of Rydberg-dressed cesium atoms. We imbue the hyperfine clock states with interactions extending over a range of several microns by coupling to Rydberg states near a Förster resonance. At the mean-field level, the Ising interactions manifest as one-axis twisting dynamics [47, 48], which we observe by Ramsey spectroscopy [2, 49]. We add an effective transverse field by pulsed application of a microwave drive. At a critical interaction-to-drive ratio, we observe a bifurcation in the mean-field dynamics which is associated with a ground-state phase transition from paramagnetic to ferromagnetic. By optically imprinting a spatially varying interaction strength, we directly observe this bifurcation as a function of position in the atomic cloud.

The principle of our experiments is illustrated in Fig. 1.

To generate Ising interactions for spins encoded in two hyperfine ground states $|\downarrow\rangle = |6S_{1/2}, F=3, m_F=0\rangle$ and $|\uparrow\rangle = |6S_{1/2}, F=4, m_F=0\rangle$, we couple state $|\uparrow\rangle$ to the Rydberg manifold $|R\rangle = |43P_{3/2}\rangle$ with a 319 nm laser field of Rabi frequency Ω and detuning Δ from the $|43P_{3/2}, m_J=3/2\rangle$ state. For large detuning $\Delta > \Omega$, the dominant effect of the dressing light on a single atom in state $|\uparrow\rangle$ is an ac Stark shift given by $\Omega^2/(4\Delta)$. However, for two atoms separated by a distance r , the ac Stark shift is modified by Rydberg interactions $V_R(r)$, which suppress a virtual process in which both atoms are simultaneously excited [Fig. 1(b)]. The result is an effective interaction $J(r)$ between atoms in state $|\uparrow\rangle$.

The ground-state dynamics are then described by an interaction Hamiltonian

$$H = \sum_{i>j} J(\mathbf{r}_i - \mathbf{r}_j) (s_i^z + 1/2) (s_j^z + 1/2), \quad (1)$$

which includes Ising interactions (terms $\propto s_i^z s_j^z$) and a density-dependent effective field (terms $\propto s_i^z$) that can be removed by spin echo. The characteristic strength of the interactions is given by $J_0 = \Omega^4/|8\Delta^3|$ (where we set $\hbar = 1$), and the sign is determined by Δ , with $\Delta > 0$ producing ferromagnetic interactions. The characteristic range r_c is set by the condition $V_R(r_c, \theta) = \Delta$ and is angle-dependent when dressing with P states [50].

To achieve a large interaction range while remaining in the dressing regime $\Delta \gg \Omega$, it is advantageous to have a strong Rydberg-Rydberg interaction. To this end, we operate in the vicinity of a Förster resonance, i.e., a near degeneracy between the energies of the $|nP_{3/2}; nP_{3/2}\rangle$ and $|nS_{1/2}; (n+1)S_{1/2}\rangle$ pair states that enhances the interaction strength [51]. We select a Rydberg state $|R\rangle$ that yields a Förster defect $\Delta_F = 2\pi \times 42$ MHz [52] and results in an interaction range $r_c \lesssim 5 \mu\text{m}$ for our typical detuning. We couple to state $|R\rangle$ with σ^+ -polarized light with respect to a quantization axis set by a 1 G magnetic field. We apply this light to a gas of cesium atoms at a temperature $T = 23 \mu\text{K}$ and typical density $\rho \sim 10^{11} \text{ cm}^{-3}$, confined in an optical dipole trap with a $50 \mu\text{m}$ waist.

We observe the Rydberg-dressed interactions by Ramsey spectroscopy. In particular, the Ising interactions in Eq. 1 cause each spin to precess at a rate that depends on the number of surrounding atoms in state $|\uparrow\rangle$. For a system of spins each initialized in state $|\theta\rangle = \sin(\theta/2)|\downarrow\rangle + \cos(\theta/2)|\uparrow\rangle$, we thus expect the average precession rate to depend on the tilt θ . We measure this effect using a spin echo sequence, shown in Fig. 2(a), which removes the s^z -independent ac Stark shift due to the dressing light and leaves behind only the phase shift resulting from Ising interactions. We extract this phase shift by fitting an interference fringe obtained by varying the phase α of the final $\pi/2$ pulse and detecting the resulting populations in states $|\uparrow\rangle$ and $|\downarrow\rangle$ by fluorescence imaging.

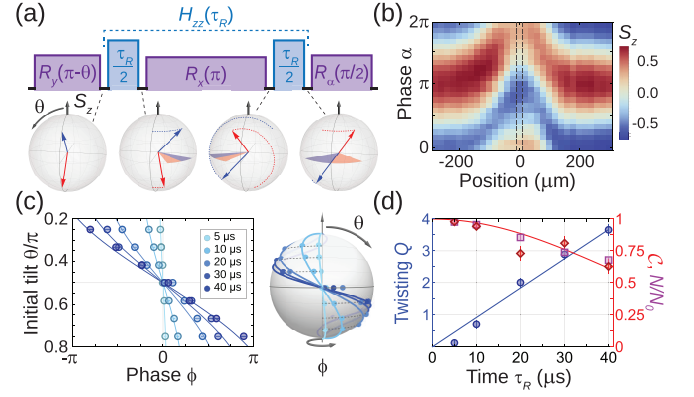


FIG. 2. Measuring Ising interactions. (a) Ramsey sequence with spin echo. Bloch spheres show average spin $\langle \mathbf{S} \rangle$ at select times for two different initial states $|\theta\rangle$ (blue and red). (b) Interference fringe for $|\theta\rangle = |3\pi/4\rangle$ showing spatial dependence of interaction-induced phase shift. Black dashed lines show analysis region for subplots (c-d). (c) Phase shift ϕ vs. initial tilt θ for different interaction times τ_R . (d) Twisting strength Q (blue circles) vs. time, extracted from fits in (c). The slope of the linear fit (solid blue) gives the mean-field interaction energy $\chi = 2\pi \times 15(1)$ kHz. Also shown are interference contrast \mathcal{C} (red diamonds with fit curve) and atom number N (magenta squares) remaining after Rydberg dressing, normalized to initial atom number N_0 .

Figure 2(b) shows a typical Ramsey fringe for determining the mean-field shift in an initial state $|\theta = 3\pi/4\rangle$. We illuminate only a $160 \mu\text{m}$ wide region of the elongated atomic cloud with the dressing light, and thus directly observe the spatial variation of the interaction strength due to the approximately Gaussian beam profile. The measurement is performed with a peak Rabi frequency $\Omega = 2\pi \times 1.9(3)$ MHz, determined from the total ac Stark shift in Ramsey measurements at large detuning without spin echo. We operate at a detuning $\Delta = 2\pi \times 21.0(3)$ MHz that empirically optimizes the ratio of coherent interactions to loss [50]. Dressing for a total time $\tau_R = 40 \mu\text{s}$ yields a peak interaction-induced phase shift $\phi = 2.6$ rad.

To more fully characterize the interactions, we perform Ramsey measurements with different initial states $|\theta\rangle$ and interaction times τ_R . We analyze the central region of the cloud, shown by the dashed lines in Fig. 2(b). The final phase ϕ of the average Bloch vector $|\theta, \phi\rangle = \sin(\theta/2)|\downarrow\rangle + e^{i\phi}\cos(\theta/2)|\uparrow\rangle$ is shown in Fig. 2(c) with different shades representing dressing times ranging from $5 \mu\text{s}$ to $40 \mu\text{s}$. We observe characteristic one-axis twisting dynamics, where the $\phi = 0$ meridian of the Bloch sphere, on which all states are initially prepared, becomes twisted about the z -axis due to the $\langle s^z \rangle$ -dependent spin precession rate.

Fitting the twisting by $\phi = Q \cos(\theta)$ yields a linear dependence of twisting strength Q on interaction time τ_R . The slope $\chi \equiv |dQ/d\tau_R| = 2\pi \times 15(1)$ kHz indicates

the mean-field interaction strength. The measured mean-field shift is approximately 3.5 times larger than the prediction $\chi_{\text{th}} = (\rho/2) \int J(\mathbf{r}) d^3\mathbf{r}$ based on the calculated interaction potential and density $\rho = 1.4 \times 10^{11} \text{ cm}^{-3}$ [50]. We attribute this to Rydberg excitations undergoing blackbody decay to nearby Rydberg states, which can effectively amplify the interaction strength, albeit in a dissipative manner. This dissipative effect can be largely echoed away in a sequence of short Rydberg pulses with more frequent π pulses, which we present further below. There, the measured interaction strength is consistent with the Rydberg-dressed potentials and atomic density.

The dynamics we observe are similar to those of the one-axis twisting Hamiltonian $H = -\chi S_z^2/N$, where $\mathbf{S} = \sum_{i=1}^N \mathbf{s}_i$ represents the collective spin of $N = 2S$ atoms. This description would be exact if the interactions had infinite range, a case well-studied as a mechanism for spin squeezing [47]. For finite-range Ising interactions, we reach a particular twisting rate via stronger pairwise interactions among fewer atoms than would be required if each atom interacted with all others. One expected consequence is a shortening of the collective Bloch vector, corresponding to a reduction in contrast $\mathcal{C} = |\langle \mathbf{S} \rangle|/S$ [48, 53]. The contrast maintained in Fig. 2(d) places a lower bound $N_c \gtrsim 14$ on the number of atoms within a typical interaction sphere [50], which corroborates the applicability of the mean-field model.

To realize the full transverse-field Ising model, we additionally apply a microwave coupling between the two ground states $|\uparrow\rangle$ and $|\downarrow\rangle$. Since we require a spin echo sequence to obtain Ising interactions $H_{ZZ} = \sum_{i>j} J(r_{ij}) s_i^z s_j^z$ with no additional ac Stark shifts, it is convenient to emulate the transverse-field Ising model by rapidly alternating between applying interactions H_{ZZ} for a time τ_R and the transverse field $H_X = \sum_i h s_i^x$ for a time τ_X . One application each of H_{ZZ} and H_X defines our Floquet cycle. When both the interaction and the rotation per Floquet cycle are small — i.e., when $\chi\tau_R \ll 1$ and $h\tau_X \ll 1$ — the effective Hamiltonian becomes equivalent to a static transverse-field Ising model:

$$H_{\text{eff}} \propto \tau_R H_{ZZ} + \tau_X H_X. \quad (2)$$

For ferromagnetic interactions, we expect the Hamiltonian H_{eff} to undergo a phase transition as a function of the ratio $\Lambda \equiv \chi\tau_R/(h\tau_X)$ of interaction strength to transverse field. When the transverse field dominates ($\Lambda \ll 1$), the ground state is paramagnetic, with all spins aligned along the x -axis. In the limit where Ising interactions dominate ($\Lambda \gg 1$), there are two degenerate ground states with all spins aligned along $\pm \hat{z}$. Even without directly preparing these ground states, we can look for signatures of the paramagnetic-ferromagnetic phase transition in the mean-field dynamics.

We probe the dynamics of the transverse-field Ising model by varying the number of Floquet cycles to measure trajectories on the Bloch sphere for different initial

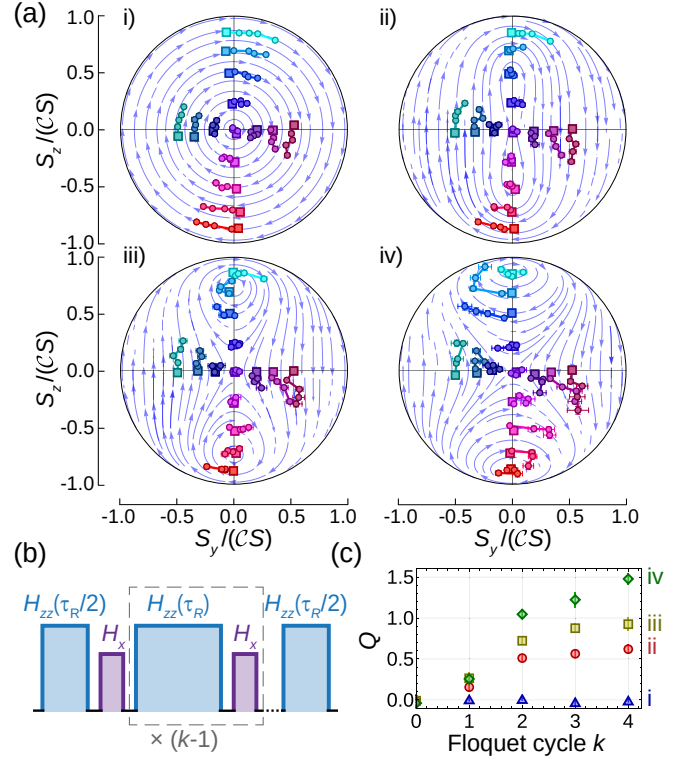


FIG. 3. **Transverse-field Ising dynamics.** (a) Trajectories $\mathbf{S}(k)$ for initial states $|\theta, \phi\rangle$ (square data points) and up to $k = 4$ Floquet cycles. Plots (i-iv) are for $\Lambda_{\text{eff}} = 0, 1.2(2), 1.8(3), 2.7(4)$. Blue flow lines show mean-field theory for best fit $\Lambda = 0, 1.1, 1.5, 2.2$. (b) Sequence of microwave (purple) and Rydberg dressing (blue) pulses for k Floquet cycles. The first application of H_{ZZ} is split into two, with the second Rydberg pulse after the last microwave rotation, to keep the fixed points along the $\phi = 0$ meridian. (c) Twisting strength Q vs. k measured with $h\tau_X = 0$ in the four regions of the atomic cloud (i-iv) used in part (a).

states [Fig. 3(a)]. After initializing in a state $|\theta, \phi\rangle$, we alternately apply Ising interactions and microwave rotations for $(\tau_R, \tau_X) = (10, 1) \mu\text{s}$. After applying up to $k = 4$ Floquet cycles as shown in Fig. 3(b), we either directly measure S_z by state-sensitive imaging or measure (S_x, S_y) by first applying a $\pi/2$ microwave pulse of variable phase. We then plot the trajectory of the normalized Bloch vector $\mathbf{S}/(CS)$. Due to the spatially varying interaction strength χ , a single such data set allows us to observe the dependence of the trajectory on χ at fixed rotation angle $h\tau_X = 0.12(1)$. The measured interaction strengths at the four representative locations shown in Fig. 3(a.i-iv) are $\chi/(2\pi) = 0, 3.2(5), 4.6(8)$, and $6.0(8)$ kHz, obtained with dressing parameters $(\Omega, \Delta) = 2\pi \times (2.8, 25)$ MHz.

We compare the observed trajectories with a mean-field model, in which the system is described by a classical Hamiltonian $H_{\text{MF}} \propto -\Lambda S_z^2/N - S_x$. The ground states of H_{MF} are fixed points of the collective spin dynamics, and

can readily be calculated for a given interaction-to-drive ratio Λ . For $\Lambda < 1$, there is only a single fixed point at $\mathbf{S} = S\hat{\mathbf{x}}$ (the paramagnetic ground state). Above a critical ratio $\Lambda = 1$, this fixed point splits into two stable fixed points (ferromagnetic ground states) at positions

$$\mathbf{S}/S = (1/\Lambda, 0, \pm\sqrt{1 - 1/\Lambda^2}), \quad (3)$$

while one unstable fixed point remains on the x -axis. Flow lines derived from this mean-field model are shown in Fig. 3(a) (blue curves).

The mean-field model qualitatively explains the dynamics we observe. Whereas the Bloch vectors precess about $\hat{\mathbf{x}}$ for weak interactions, above a critical interaction strength they instead begin to precess about two new fixed points in the xz -plane. For a quantitative comparison, we must account for effects of dissipation and interaction-induced dephasing. First, we observe a decrease in interaction strength χ for later Floquet cycles [Fig. 3(c)], which we attribute to loss and decay of Rydberg atoms. The given values of χ are the averages over the four Floquet cycles. Second, we observe a reduction in contrast \mathcal{C} , whose effect on the fixed-point positions is described by replacing Λ in Eq. 3 by $\Lambda_{\text{eff}} \equiv \mathcal{C}\Lambda$ [50]. Independently measured values of Λ_{eff} are within 20% of values obtained by fitting the mean-field model to the trajectories.

The spatially varying interaction strength allows us to directly observe the paramagnetic-ferromagnetic phase transition as a function of position in the atomic cloud. In Fig. 4(a), we observe the spatial dependence of the phase ϕ after four Floquet cycles for different initial states $|\theta\rangle$. Fixed points are revealed by the white contour level, where $\phi = 0$. Outside of the dressing beam (e.g., at position A), a single fixed point is visible at $\theta = \pi/2$. At a critical interaction strength, theoretically given by $\mathcal{C}\chi\tau_R = h\tau_X$, the stable fixed point bifurcates and all three fixed points become visible.

To compare the position of the critical point with theory, we calibrate the spatial dependence of the interaction strength by an analogous measurement with no transverse field [Fig. 4(b)]. We plot and fit the spatial dependence of $\mathcal{C}\chi\tau_R$ in Fig. 4(c), accounting for the spatially varying contrast $\mathcal{C} \gtrsim 0.7$. Comparing with the value $h\tau_X = 0.14(1)$ yields a prediction for the positions of the fixed points shown by the dashed green curve in Fig. 4(a). In Fig. 4(d), we furthermore compare the full dependence of final phase ϕ on initial tilt θ with a mean-field model of the Floquet sequence. This model is shown by the solid curves, which incorporate the independently measured values $\chi\tau_R$ and $h\tau_X$ and include only a small phase offset as a free parameter. The full phase evolution, including the fixed-point positions, is well described by the mean-field model.

The dynamical timescales accessible in our current experiments are limited by atom loss and by motion into

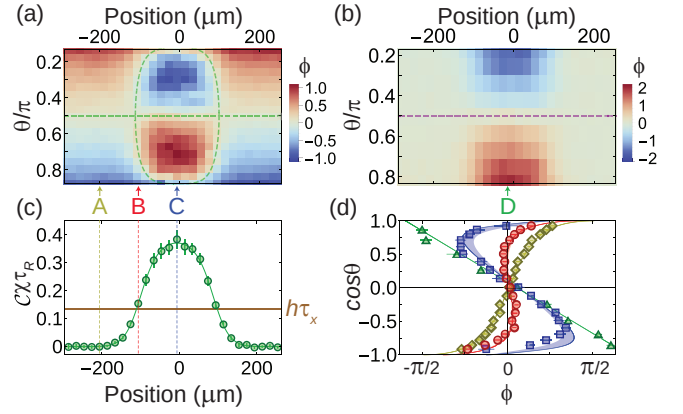


FIG. 4. Inhomogeneous phase transition. Phase ϕ after $k = 4$ cycles of the Floquet transverse-field Ising model with (a) $h\tau_X = 0.14(1)$ or (b) $h\tau_X = 0$, as a function of initial tilt θ and position. Fitting the phase evolution in (b) yields the average mean-field interaction $\chi\tau_R$ per cycle. (c) Green points and fit curve show $\mathcal{C}\chi\tau_R$ vs. position, compared with rotation angle $h\tau_X$ (brown line). (d) Final phase ϕ vs. initial tilt θ for cuts labeled A (yellow diamonds), B (red circles), C (blue squares), and D (green triangles), in order of increasing $|\Lambda|$. Solid lines show Floquet mean-field model for the measured values $\chi\tau_R$ and $h\tau_X$ with no contrast loss, while edge of shaded region accounts for contrast \mathcal{C} .

and out of the dressing region. Both of these effects can be reduced in future experiments by trapping the atoms in a lattice or tweezer array, where the discretization of interatomic spacings helps to avoid avalanche decay effects triggered by blackbody radiation [3]. Future work may also explore the use of electric fields, molecular bound states [13, 54], microwave dressing [55] and/or adiabatic protocols [56] to achieve interaction-to-decay ratios exceeding 10^3 , limited only by the ratio of Rabi frequency to Rydberg state linewidth.

Our work opens prospects in quantum simulation benefiting from spatiotemporal control of interactions, including exploring quantum criticality in both driven [27] and spatially inhomogeneous [29] systems. Whereas here we have emulated a static transverse-field Ising model, varying the strength of interaction and/or rotation per Floquet cycle will allow for accessing quantum phases with no equilibrium analog [26, 57], including Floquet symmetry-protected topological phases [14, 26]. Combining Floquet driving with a spatially varying interaction strength may allow for realizing quantum systems with emergent spacetime curvature [58]. The Ising interactions demonstrated here can furthermore be applied to generate entangled states for enhanced clocks or sensors [32, 48], with optimal dynamical control of interactions and the transverse field enabling enhanced spin squeezing [34]. Spatial addressing will additionally allow for preparing arrays of entangled states for optimal atomic clocks [59, 60].

This work was supported by the ARO and the ONR. V. Borish acknowledges support from the NSF GRFP and the DARE Doctoral Fellowship. O. Marković acknowledges support from the Serbian Foundation for Talented Youth. J. Hines acknowledges support from the NDSEG Fellowship. J. Hines and M. Schleier-Smith acknowledge support from the DOE Office of Science, Office of Basic Energy Sciences, under grant number DE-SC0019174. We acknowledge technical assistance from Michelle Chong and Josie Meyer and discussions with Leo Hollberg.

-
- [1] P. Schauß, M. Cheneau, M. Endres, T. Fukuhara, S. Hild, A. Omran, T. Pohl, C. Gross, S. Kuhr, and I. Bloch, *Nature* **491**, 87 (2012).
- [2] J. Zeiher, R. Van Bijnen, P. Schauß, S. Hild, J.-y. Choi, T. Pohl, I. Bloch, and C. Gross, *Nat. Phys.* **12**, 1095 (2016).
- [3] J. Zeiher, J.-Y. Choi, A. Rubio-Abadal, T. Pohl, R. van Bijnen, I. Bloch, and C. Gross, *Phys. Rev. X* **7**, 041063 (2017).
- [4] H. Labuhn, D. Barredo, S. Ravets, S. De Léséleuc, T. Macrì, T. Lahaye, and A. Browaeys, *Nature* **534**, 667 (2016).
- [5] H. Bernien, S. Schwartz, A. Keesling, H. Levine, A. Omran, H. Pichler, S. Choi, A. S. Zibrov, M. Endres, M. Greiner, et al., *Nature* **551**, 579 (2017).
- [6] S. de Léséleuc, V. Lienhard, P. Scholl, D. Barredo, S. Weber, N. Lang, H. P. Büchler, T. Lahaye, and A. Browaeys, *Science* **365**, 775 (2019).
- [7] A. P. Orioli, A. Signoles, H. Wildhagen, G. Günter, J. Berges, S. Whitlock, and M. Weidemüller, *Phys. Rev. Lett.* **120**, 063601 (2018).
- [8] M. Landini, N. Dogra, K. Kröger, L. Hruby, T. Donner, and T. Esslinger, *Phys. Rev. Lett.* **120**, 223602 (2018).
- [9] Y. Guo, R. M. Kroeze, V. D. Vaidya, J. Keeling, and B. L. Lev, *Phys. Rev. Lett.* **122**, 193601 (2019).
- [10] E. J. Davis, G. Bentsen, L. Homeier, T. Li, and M. H. Schleier-Smith, *Phys. Rev. Lett.* **122**, 010405 (2019).
- [11] M. Yan, B. J. DeSalvo, B. Ramachandran, H. Pu, and T. C. Killian, *Phys. Rev. Lett.* **110**, 123201 (2013).
- [12] O. Thomas, C. Lippe, T. Eichert, and H. Ott, *Nat. Commun.* **9**, 2238 (2018).
- [13] R. M. W. van Bijnen and T. Pohl, *Phys. Rev. Lett.* **114**, 243002 (2015).
- [14] I.-D. Potirniche, A. C. Potter, M. Schleier-Smith, A. Vishwanath, and N. Y. Yao, *Phys. Rev. Lett.* **119**, 123601 (2017).
- [15] G. Pupillo, A. Micheli, M. Boninsegni, I. Lesanovsky, and P. Zoller, *Phys. Rev. Lett.* **104**, 223002 (2010).
- [16] J. E. Johnson and S. L. Rolston, *Phys. Rev. A* **82**, 033412 (2010).
- [17] N. Henkel, R. Nath, and T. Pohl, *Phys. Rev. Lett.* **104**, 195302 (2010).
- [18] E. Urban, T. A. Johnson, T. Henage, L. Isenhower, D. D. Yavuz, T. G. Walker, and M. Saffman, *Nat. Phys.* **5**, 110 (2009).
- [19] A. Gaëtan, Y. Miroshnychenko, T. Wilk, A. Chotia, M. Viteau, D. Comparat, P. Pillet, A. Browaeys, and P. Grangier, *Nat. Phys.* **5**, 115 (2009).
- [20] X. L. Zhang, L. Isenhower, A. T. Gill, T. G. Walker, and M. Saffman, *Phys. Rev. A* **82**, 030306(R) (2010).
- [21] T. Wilk, A. Gaëtan, C. Evellin, J. Wolters, Y. Miroshnychenko, P. Grangier, and A. Browaeys, *Phys. Rev. Lett.* **104**, 010502 (2010).
- [22] Y.-Y. Jau, A. M. Hankin, T. Keating, I. H. Deutsch, and G. W. Biedermann, *Nat. Phys.* **12**, 71 (2016).
- [23] I. D. Leroux, M. H. Schleier-Smith, and V. Vuletić, *Phys. Rev. Lett.* **104**, 073602 (2010).
- [24] O. Hosten, R. Krishnakumar, N. J. Engelsen, and M. A. Kasevich, *Science* **352**, 1552 (2016).
- [25] I. Bouchoule and K. Mølmer, *Phys. Rev. A* **65**, 041803(R) (2002).
- [26] V. Khemani, A. Lazarides, R. Moessner, and S. L. Sondhi, *Phys. Rev. Lett.* **116**, 250401 (2016).
- [27] W. Berdanier, M. Kolodrubetz, S. Parameswaran, and R. Vasseur, *Proc. Natl. Acad. Sci. U.S.A.* **115**, 9491 (2018).
- [28] A. Lerose, J. Marino, A. Gambassi, and A. Silva, *Phys. Rev. B* **100**, 104306 (2019).
- [29] F. J. Gómez-Ruiz and A. del Campo, *Phys. Rev. Lett.* **122**, 080604 (2019).
- [30] A. W. Glaetzle, R. M. van Bijnen, P. Zoller, and W. Lechner, *Nat. Commun.* **8**, 15813 (2017).
- [31] H. Pichler, S.-T. Wang, L. Zhou, S. Choi, and M. D. Lukin, arXiv:1808.10816 [quant-ph] (2018).
- [32] E. Davis, G. Bentsen, and M. Schleier-Smith, *Phys. Rev. Lett.* **116**, 053601 (2016).
- [33] T. Macrì, A. Smerzi, and L. Pezzè, *Phys. Rev. A* **94**, 010102(R) (2016).
- [34] R. Kaubruegger, P. Silvi, C. Kokail, R. van Bijnen, A. M. Rey, J. Ye, A. M. Kaufman, and P. Zoller, arXiv:1908.08343 [quant-ph] (2019).
- [35] F. K. Fatemi, K. M. Jones, and P. D. Lett, *Phys. Rev. Lett.* **85**, 4462 (2000).
- [36] G. Thalhammer, M. Theis, K. Winkler, R. Grimm, and J. H. Denschlag, *Phys. Rev. A* **71**, 033403 (2005).
- [37] K. Enomoto, K. Kasa, M. Kitagawa, and Y. Takahashi, *Phys. Rev. Lett.* **101**, 203201 (2008).
- [38] S. Blatt, T. L. Nicholson, B. J. Bloom, J. R. Williams, J. W. Thomsen, P. S. Julienne, and J. Ye, *Phys. Rev. Lett.* **107**, 073202 (2011).
- [39] C. Gaul, B. J. DeSalvo, J. A. Aman, F. B. Dunning, T. C. Killian, and T. Pohl, *Phys. Rev. Lett.* **116**, 243001 (2016).
- [40] E. A. Goldschmidt, T. Boulier, R. C. Brown, S. B. Koller, J. T. Young, A. V. Gorshkov, S. L. Rolston, and J. V. Porto, *Phys. Rev. Lett.* **116**, 113001 (2016).
- [41] T. Boulier, E. Magnan, C. Bracamontes, J. Maslek, E. A. Goldschmidt, J. T. Young, A. V. Gorshkov, S. L. Rolston, and J. V. Porto, *Phys. Rev. A* **96**, 053409 (2017).
- [42] J. A. Aman, B. J. DeSalvo, F. B. Dunning, T. C. Killian, S. Yoshida, and J. Burgdörfer, *Phys. Rev. A* **93**, 043425 (2016).
- [43] T. Zibold, E. Nicklas, C. Gross, and M. K. Oberthaler, *Phys. Rev. Lett.* **105**, 204101 (2010).
- [44] A. Friedenauer, H. Schmitz, J. T. Glueckert, D. Porras, and T. Schätz, *Nat. Phys.* **4**, 757 (2008).
- [45] R. Islam, E. E. Edwards, K. Kim, S. Korenblit, C. Noh, H. Carmichael, G.-D. Lin, L.-M. Duan, C.-C. J. Wang, J. K. Freericks, et al., *Nat. Commun.* **2**, 377 (2011).
- [46] J. Zhang, P. Hess, A. Kyprianidis, P. Becker, A. Lee, J. Smith, G. Pagano, I.-D. Potirniche, A. C. Potter,

- A. Vishwanath, *et al.*, *Nature* **543**, 217 (2017).
- [47] M. Kitagawa and M. Ueda, *Phys. Rev. A* **47**, 5138 (1993).
 - [48] L. I. R. Gil, R. Mukherjee, E. M. Bridge, M. P. A. Jones, and T. Pohl, *Phys. Rev. Lett.* **112**, 103601 (2014).
 - [49] R. Mukherjee, T. C. Killian, and K. R. A. Hazzard, *Phys. Rev. A* **94**, 053422 (2016).
 - [50] See Supplemental Material at [URL will be inserted by publisher] for supporting derivations and additional experimental details.
 - [51] T. Vogt, M. Viteau, J. Zhao, A. Chotia, D. Comparat, and P. Pillet, *Phys. Rev. Lett.* **97**, 083003 (2006).
 - [52] N. Šibalić, J. D. Pritchard, K. J. Weatherill, and C. S. Adams, *Comput. Phys. Commun.* **220**, 319 (2017).
 - [53] M. Foss-Feig, K. R. A. Hazzard, J. J. Bollinger, and A. M. Rey, *Phys. Rev. A* **87**, 042101 (2013).
 - [54] S. Hollerith, J. Zeiher, J. Rui, A. Rubio-Abadal, V. Walther, T. Pohl, D. M. Stamper-Kurn, I. Bloch, and C. Gross, *Science* **364**, 664 (2019).
 - [55] D. Petrosyan and K. Mølmer, *Phys. Rev. Lett.* **113**, 123003 (2014).
 - [56] T. Keating, R. L. Cook, A. M. Hankin, Y.-Y. Jau, G. W. Biedermann, and I. H. Deutsch, *Phys. Rev. A* **91**, 012337 (2015).
 - [57] D. V. Else, B. Bauer, and C. Nayak, *Phys. Rev. Lett.* **117**, 090402 (2016).
 - [58] B. Lapierre, K. Choo, C. Tauber, A. Tiwari, T. Neupert, and R. Chitra, *arXiv:1909.08618 [cond-mat.str-el]* (2019).
 - [59] E. M. Kessler, P. Komar, M. Bishof, L. Jiang, A. S. Sørensen, J. Ye, and M. D. Lukin, *Phys. Rev. Lett.* **112**, 190403 (2014).
 - [60] V. Bužek, R. Derka, and S. Massar, *Phys. Rev. Lett.* **82**, 2207 (1999).

Transverse-Field Ising Dynamics in a Rydberg-Dressed Atomic Gas: Supplemental Material

In this supplement, we provide additional details of the experimental methods and the theoretical models with which we compare the data in the main text. In Sec. I, we elaborate on the experimental apparatus, sequence, and data analysis, and present supporting measurements of Rydberg-dressed interactions and their dependence on laser parameters. Section II provides supporting theoretical background, including calculations of interaction potentials and a derivation of the mean-field model.

I. EXPERIMENTAL DETAILS

A. Atomic state preparation

The experimental sequence begins with two-stage cooling of cesium atoms, consisting of a 2D magneto-optical trap (MOT) and a 3D MOT, over a period of 1.5 s. After a bright optical molasses stage, the atoms are loaded into a 1064 nm optical dipole trap with a 50 μm waist and a trap depth $\hbar \times 3(1)$ MHz. The atoms are then transported over a distance of 37 cm, by shifting the focus of the dipole trap using an electrically tunable lens [1], to a science chamber where our experiments are performed. After transport, the atoms are optically pumped in a ~ 5 G magnetic field along the dipole trap direction into the state $|6S_{1/2}, F=4, m_F=4\rangle$. The magnetic field is subsequently reduced to 1 G and atoms are transferred to state $|\downarrow\rangle = |6S_{1/2}, F=3, m_F=0\rangle$ by an adiabatic sweep of a microwave field. We then apply a resonant light pulse on the $|6S_{1/2}, F=4\rangle \rightarrow |6P_{3/2}, F'=5\rangle$ transition to remove all residual $F=4$ atoms.

B. Rydberg dressing and microwave parameters

To generate the 319 nm Rydberg dressing light, we start from a diode laser at 1276 nm that is used to seed a Raman fiber amplifier. Light from the amplifier is resonantly doubled in two stages (LEOS Solutions), each consisting of a nonlinear crystal in a bow-tie optical cavity. The frequency of the 319 nm light is stabilized by locking the seed laser to a stable reference cavity. The focused dressing laser beam has a waist of 80 μm and, due to its incidence angle of 30 degrees with respect to the optical dipole trap axis, effectively addresses a 160 μm region of the atom cloud. For a power of ~ 320 mW, we measure a Rabi frequency $\Omega = 2\pi \times 2.8$ MHz.

We always apply the Rydberg light in a spin echo sequence consisting of two pulses separated by approximately 30 μs . This is enough time for a π pulse with our typical microwave Rabi frequencies of $\Omega_{\text{MW}} = 2\pi \times 25$ kHz for Fig. 2 in the main text and $\Omega_{\text{MW}} = 2\pi \times 18$ kHz for Figs. 3 and 4 in the main text.

C. Detection and analysis

To perform state-sensitive fluorescence imaging, we first use light tuned to the $|F=4\rangle \rightarrow |F'=5\rangle$ transition to image only the $|F=4\rangle$ atoms. After this, we reapply the same pulse to resonantly expel any remaining $|F=4\rangle$ atoms. We then reapply the resonant light and add light tuned to the $|F=3\rangle \rightarrow |F'=4\rangle$ transition to repump and image the atoms that were initially in $|F=3\rangle$. During imaging, we observe that approximately 7% of $|F=4\rangle$ atoms also appear in the $|F=3\rangle$ image due to a combination of off-resonant depumping during the first two pulses and imperfect expulsion. Additionally we find 5% of all atoms in $|F=3, m_F \neq 0\rangle$ states due to imperfect optical pumping; these atoms do not contribute to the experiment, as they are not affected by microwave pulses or Rydberg dressing light. We account for both of the above effects in our calibration of the population difference $2S_z$ between states $|F=4, m_F=0\rangle$ and $|F=3, m_F=0\rangle$.

We integrate the atomic signal over the transverse direction of the elongated atomic cloud. This averages atomic sub-ensembles experiencing slightly different intensities of dressing light as the 319 nm laser beam is not perpendicular to the atomic cloud. We bin the longitudinal direction of the cloud in 20 μm regions, a size comparable to the ~ 10 μm scale of thermal motion during imaging. In addition to this thermal motion, we observe center-of-mass motion on the scale of 60 $\mu\text{m/ms}$ due to residual momentum from transport in the dipole trap and additional momentum imparted by the optical pumping light. To limit the effects of motion on our experiments, we restrict the total duration of the Ramsey and Floquet sequences to at most 325 μs .

D. Measuring Rydberg-dressed interactions

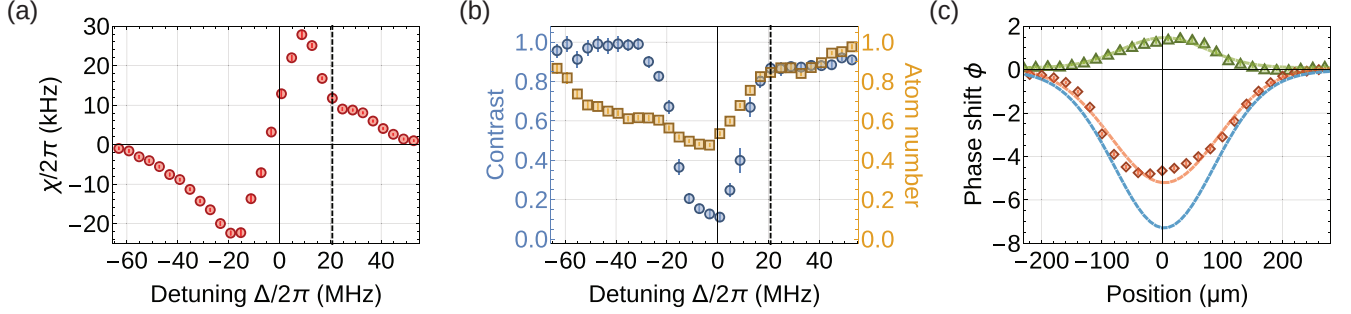


FIG. S1. **Optimizing Rydberg dressing parameters.** (a) Mean-field interaction strength χ vs. detuning Δ . The dressing light was applied for a total of $\tau_R = 40 \mu\text{s}$. The gray dashed line shows the detuning chosen for the measurement of Ising interactions in Fig. 2 of the main text. (b) Contrast (blue circles) and normalized atom number (yellow squares) after the application of dressing light for $\tau_R = 40 \mu\text{s}$. (c) Total ac Stark shift measured for initial state $|\theta\rangle = |\pi/2\rangle$ (orange diamonds), compared with interaction shift for initial state $|\theta\rangle = |3\pi/4\rangle$ (green triangles), after 20 μs of Rydberg dressing at $\Delta = 2\pi \times 19.5$ MHz. The green and orange lines are Gaussian fits to the data, which are used to extrapolate the total ac Stark shift in the limit of a dilute system (blue line).

To identify optimal parameters for Rydberg dressing, we measure the mean-field shift as a function of detuning Δ from the $|43P_{3/2}, m_J = 3/2\rangle$ state, as shown in Fig. S1(a). To do so, we initialize the atoms in one of two spin-polarized states $|\theta_{\pm}\rangle = |\pi/2 \pm \pi/4\rangle$ tilted either above or below the equator of the Bloch sphere. After applying the dressing light for a total time $\tau_R = 40 \mu\text{s}$ in the Ramsey sequence with spin echo, we measure the difference in phase shift $\phi_{\pm} - \phi_0$ between the Rydberg-dressed region and a reference region of the cloud that is unaffected by the dressing light. We thus obtain the mean-field interaction strength $\chi = \frac{\phi_{+} - \phi_{-}}{\sqrt{2}\tau_R}$.

While for small detunings $|\Delta|$ the measurements are dominated by loss, at larger detunings we observe a strong interaction-induced phase shift while the atom number and interference contrast remain high [Fig. S1(b)]. For the Ising interaction data in the main text, we chose to work at a detuning $\Delta = 2\pi \times 21.0(3)$ MHz. On the red-detuned side of the Rydberg state resonance we observe slightly smaller interaction strength but higher atom loss extending to larger detunings due to resonant coupling to the doubly-excited $|43P_{3/2}; 43P_{3/2}\rangle$ state.

To assess whether we are working in a perturbative dressing regime, we compare the interaction phase shift to the total light shift, as shown in Fig. S1(c). We measure the total light shift for the state $|\theta = \pi/2\rangle$ by Ramsey spectroscopy without spin echo (orange diamonds). Based on our measurement of the interaction shift under the same parameters with initial state $|\theta = 3\pi/4\rangle$ (green triangles), we can extrapolate the total light shift in the limit of a dilute system (blue curve). Comparing the blue and orange curves shows a 30% suppression of the light shift for the state $|\theta = \pi/2\rangle$. This is a small enough fraction for a perturbative analysis of the dressing to be approximately valid.

E. Rydberg interaction range

To deduce whether the contrast decay we observe in our experiment results from the finite interaction range, we compare the data in Fig. 2(d) with a theoretical model of contrast decay as a function of twisting strength $Q(\tau_R)$. We consider one spin interacting with N_c other spins with a pairwise interaction strength that is constant within the interaction radius and zero everywhere else. This enables us to derive an analytic expression $\mathcal{C} = \langle S_x \rangle / S = \cos(Q/N_c)^{N_c}$ for the contrast [2], which we can use to find the best-fit N_c from the decaying contrast data. As shown in Fig. 2 in the main text, we fit $N_c = 14$. We interpret this as a lower bound on the number of atoms within the interaction range, since a shorter-range interaction would result in faster contrast decay. For comparison, we estimate that the actual number of atoms within the interaction range is $N_c \sim 30$, based on the density, calculated dressed potentials, and mean-field interaction strength measured in the Floquet sequences. Thus, the observed contrast decay is only partially accounted for by the finite interaction range.

F. Fitting the mean-field model to measured trajectories

To fit the values of Λ in the mean-field model to the transverse-field Ising dynamics data presented in the main text [Fig. 3(a)], we extract the positions of the fixed points θ_{fix} where $\dot{\phi} = 0$. We fit a third order polynomial to the final ϕ vs. initial θ for different numbers of Floquet cycles and regions of interest. We average θ_{fix} over different numbers of Floquet cycles to arrive at our final fit value of Λ , using Eq. S12, for each region of interest.

II. THEORY

A. Interaction potentials

In order to calculate the dressed ground state interaction potentials, we first calculate the Rydberg pair state potentials with the Alkali Rydberg Calculator (ARC) [3] and then use perturbation theory as in Ref. [4] to calculate the dressed potentials.

We calculate the Rydberg pair potentials by exact diagonalization of the dipole-dipole interaction Hamiltonian for Rydberg pair states $|\alpha\alpha'\rangle \equiv |n, L, J, m_J; n', L', J', m_{J'}\rangle$. We include pair states with $41 \leq n, n' \leq 45$, $0 \leq L, L' \leq 3$, and a maximum energy difference of 20 GHz between the pair state and $|43P_{3/2}, m_J = -\frac{1}{2}\rangle; |43P_{3/2}, m_J = \frac{1}{2}\rangle$. The ranges were chosen to ensure convergence of the dressed potentials. A magnetic field of 1 G defining the quantization axis is included in these calculations to match the experiment. Since the interaction potentials are anisotropic, we show Rydberg pair potentials for $\varphi = 0$ and $\varphi = \pi/2$, where φ is the angle between the quantization axis and the interatomic axis [Fig. S2(a)]. The coloring of the pair states is the two-photon Rabi frequency $\Omega_{\psi(r)}$ between $|\uparrow\uparrow\rangle$ and the Rydberg pair eigenstate $|\psi(r)\rangle$:

$$\Omega_{\psi(r)} = \sum_{\alpha, \alpha'} \langle \psi(r) | \alpha\alpha' \rangle \frac{\Omega_{\uparrow\alpha} \Omega_{\uparrow\alpha'}}{2} \left(\frac{1}{\omega_L + (E_{\uparrow} - E_{\alpha})/\hbar} + \frac{1}{\omega_L + (E_{\uparrow} - E_{\alpha'})/\hbar} \right). \quad (\text{S1})$$

In this equation, r is the distance between the two atoms, ω_L is the frequency of the dressing laser, E_{\uparrow} and E_{α} are single-atom energies, and $\Omega_{\uparrow\alpha}$ is the single-atom Rabi frequency between $|\uparrow\rangle = |6S_{1/2}, F=4, m_F=0\rangle$ and $|\alpha\rangle$.

The effect of the Rydberg interactions on the energy of a pair of ground-state atoms $|\uparrow\uparrow\rangle$ arises at fourth order in perturbation theory. We can understand it as a reduction in the total ac-Stark shift when the Rydberg-Rydberg interactions cause $|\psi(r)\rangle$ to be shifted out of resonance with the dressing light. The energy shift U of $|\uparrow\uparrow\rangle$ is

$$U(r) = \frac{\hbar}{4} \sum_{\psi(r)} \frac{|\Omega_{\psi(r)}|^2}{2\omega_L - E_{\psi(r)}/\hbar}, \quad (\text{S2})$$

where $E_{\psi(r)}$ are the energies of the Rydberg pair eigenstates. Since our ground state $|\uparrow\rangle$ is a superposition of two states with different nuclear spin, we must account for both nuclear spin states. We write our ground state as $|\uparrow\rangle = \frac{1}{\sqrt{2}} (|6S_{1/2}, m_J = \frac{1}{2}, m_I = -\frac{1}{2}\rangle + |6S_{1/2}, m_J = -\frac{1}{2}, m_I = \frac{1}{2}\rangle)$. The σ^+ dressing laser couples this state to both $|43P_{3/2}, m_J = 3/2, m_I = -1/2\rangle$ and $|43P_{3/2}, m_J = 1/2, m_I = 1/2\rangle$. Our measured Rabi frequency has contributions from both of these states, so we account for the state coefficients and the relative dipole matrix elements in our calculations of the Rabi frequencies $\Omega_{\uparrow\alpha}$.

Figure S2(b) shows representative dressed potentials $J(r) = [U(r) - U(\infty)]/\hbar$ for $\varphi = 0, \pi/2$ and three pairs of detunings and Rabi frequencies $(\Omega, \Delta)/(2\pi) = (1.9, 21)$ MHz, $(2.8, 25.3)$ MHz, and $(2, 16)$ MHz, which correspond to the data in Fig. 2, the data in Fig. 3, and a reference calculation, respectively. The detunings used for the measurements in the main text were greater than half the Förster defect Δ_F . This means that for some distance r , the laser is on two-photon resonance with the $|43S_{1/2}; 44S_{1/2}\rangle$ pair state that is hybridized with the nearly Förster-resonant P states. This causes sharp resonances in the calculated dressed potentials. We expect these resonances to be averaged out by atomic motion, as illustrated schematically in Fig. 1 in the main text. The reference calculation with $\Delta = 2\pi \times 16$ MHz $< \Delta_F/2$ shows the shape of a similar dressed potential without resonances. Experimentally, we do not see a noticeable difference in interaction strength with similar parameters at nearby states of principal quantum number n where $\Delta < \Delta_F/2$. Thus, we infer that the resonances do not appreciably affect the mean field felt by each atom.

In order to estimate the theoretical mean-field energy shift on an atom, we find an (Ω, Δ) pair that gives the same J_0 values as that from the measured Rabi frequency and detuning. This gives a reference potential that is similar in shape to a smoothed version of the potential for our experimental values of Ω and Δ . We calculate these potentials for 100 different angles $0 \leq \varphi \leq \pi$ and integrate under these curves in three dimensions (accounting for the 2π symmetry in

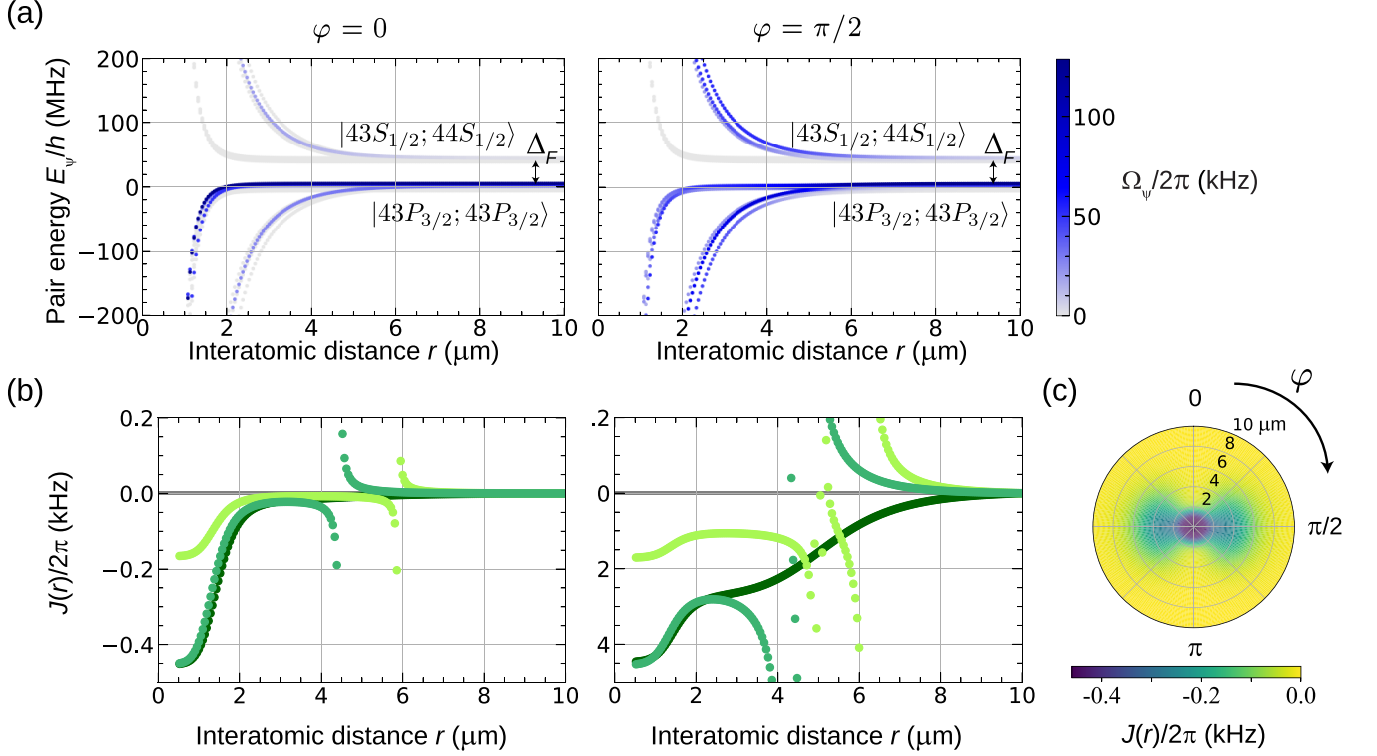


FIG. S2. **Interaction potentials.** (a) Rydberg pair potentials calculated by exact diagonalization for $\varphi = 0$ and $\varphi = \pi/2$. The coloring is the two-photon Rabi frequency between $|\uparrow\uparrow\rangle$ and the pair eigenstate. (b) Dressed potentials for our experimental parameters at $\varphi = 0$ and $\varphi = \pi/2$. Potentials are calculated for $(\Omega, \Delta)/(2\pi) = (1.9, 21)$ MHz (light green), $(2.8, 25.3)$ MHz (medium green), and $(2, 16)$ MHz (dark green). The parameters for the light and medium green curves match Fig. 2 and Fig. 3, respectively, of the main paper. The dark green shows a representative shape of the potential in the absence of the resonances. (c) Plot of dressing potential by distance r and angle φ for $(\Omega, \Delta)/(2\pi) = (2, 16)$ MHz.

the azimuthal angle). We thus obtain the theoretical prediction $\chi_{\text{th}} = -(\rho/2) \int J(\mathbf{r}) d^3\mathbf{r}$ for the measured interaction strength at density ρ , based on the relationship between χ and J derived in Sec. II B. We perform this calculation with two separate reference potentials, one for the data in Fig. 2 and one for the data in Fig. 3.

B. Derivation of mean-field model

To derive an effective Hamiltonian governing the spin dynamics in our experiment, we first consider N spins subject to the Ising Hamiltonian

$$H = \frac{1}{2} \sum_{i,j \neq i} J_{ij} s_i^z s_j^z, \quad (\text{S3})$$

where $J_{ij} = J(\mathbf{r}_i - \mathbf{r}_j)$ is the interaction strength between spins i and j and we set $\hbar = 1$. This Hamiltonian governs the dynamics of the spins in our experiment under the condition that we cancel out any terms linear in s^z by using a spin echo sequence. To understand the spin dynamics, it is sufficient to look at the time dynamics of the s^{\pm} operators because the Ising Hamiltonian conserves all s^z .

We analyze the dynamics in the Heisenberg picture where the time dependence of the operator s_n^{\pm} for spin n is given by

$$\dot{s}_n^\pm = i [H, s_n^\pm] \quad (\text{S4a})$$

$$= \frac{i}{2} \sum_{i,j \neq n} J_{ij} (s_i^z [s_j^z, s_n^\pm] + [s_i^z, s_n^\pm] s_j^z) \quad (\text{S4b})$$

$$= \pm i \sum_{i \neq n} J_{in} s_i^z s_n^\pm. \quad (\text{S4c})$$

Defining the total spin of N atoms in a designated region of the atomic cloud as $\mathbf{S} = \sum_n \mathbf{s}_n$ and summing the previous equation, we obtain:

$$\dot{S}_\pm = \pm i \sum_n \sum_{i \neq n} J_{in} s_i^z s_n^\pm. \quad (\text{S5})$$

In the limit where each spin interacts with many neighboring spins around it, a lowest-order approximation is to replace s_i^z with its mean value $\langle s_i^z \rangle$, ignoring quantum fluctuations and correlations. Note that this number of neighboring spins is smaller than the total number of atoms N considered, due to the finite interaction range. Under the additional assumption that all N spins in the region of interest are subject to the same environment (i.e., same average density and polarization of the surrounding spins), we can write $\langle s_i^z \rangle = \frac{\sum_j \langle s_j^z \rangle}{N} = \frac{\langle S_z \rangle}{N}$. In the limit of large total spin S we can make a substitution $\langle S_z \rangle = S_z$ leading to:

$$\dot{S}_\pm \approx \pm \frac{i S_z}{N} \sum_n \sum_{i \neq n} J_{in} s_n^\pm. \quad (\text{S6})$$

Finally, we define χ in terms of the sum of the interaction strengths:

$$\chi \equiv \chi_n = -\frac{1}{2} \sum_{i \neq n} J_{in}, \quad (\text{S7})$$

where we choose a sign convention such that χ is positive for the ferromagnetic interactions studied here. We thus obtain the equation governing the mean-field dynamics of S_\pm :

$$\dot{S}_\pm \approx \mp \frac{2i\chi}{N} S_z S_\pm. \quad (\text{S8})$$

The dynamics derived here are the same as those under the one-axis twisting Hamiltonian $H = -\frac{\chi}{N} S_z^2$ [5].

To relate χ to the measured twisting strength Q , we can derive the dynamics of the S_\pm operators from Equation S8:

$$S_\pm(t) = e^{\mp \frac{2i\chi}{N} S_z t} S_\pm(0). \quad (\text{S9})$$

The phase $\phi = \frac{2\chi}{N} S_z t$ directly corresponds to the phase of the average Bloch vector evolving under the Ising Hamiltonian in our experiment. Substituting $N = 2S$ in this equation, we find $\phi = \chi t \frac{S_z}{S} = \chi t \cos \theta$. More generally, even if the interaction strength χ is time dependent, we obtain $\dot{\phi} = \chi(t) \cos \theta$. Using the definition of Q from the main text, where $\phi = Q \cos \theta$, we arrive at the relation $\chi = \left| \dot{Q} \right|$.

C. Fixed points of the transverse-field Ising model

To calculate the fixed points of the transverse-field Ising model in the mean-field limit, we consider the dynamics of the Hamiltonian derived in the previous section with an added global transverse field:

$$H = -\frac{\chi}{N} S_z^2 - h S_x. \quad (\text{S10})$$

From the Heisenberg equation of motion $\dot{\mathbf{S}} = i[H, \mathbf{S}]$, we determine the time evolution of each spin component:

$$\dot{S}_x = -i\frac{\chi}{N}[S_z^2, S_x] = \frac{\chi}{N}(S_z S_y + S_y S_z) \quad (\text{S11a})$$

$$\dot{S}_y = -i\frac{\chi}{N}[S_z^2, S_y] - ih[S_x, S_y] = -\frac{\chi}{N}(S_z S_x + S_x S_z) + hS_z \quad (\text{S11b})$$

$$\dot{S}_z = -ih[S_x, S_z] = -hS_y. \quad (\text{S11c})$$

To find fixed points, we solve for $\dot{\mathbf{S}} = 0$. From $\dot{S}_z = 0$, it follows that all fixed points have $S_y = 0$. From $\dot{S}_y = 0$, we have $S_z = 0$ or $S_x = \frac{hN}{2\chi} = \frac{hS}{\chi}$. For non-trivial fixed points at $S_z \neq 0$ to exist, the mean-field interaction strength and the transverse field must satisfy $h/\chi \leq 1$, with the critical point at $h = \chi$.

It is thus natural to define the parameter $\Lambda = \frac{\chi}{h}$, which fully determines the dynamics of the normalized Bloch vectors \mathbf{S}/S , including the critical point at $\Lambda = 1$ and the positions of the fixed points. The coordinates of the fixed points are then given by

$$\mathbf{S}/S = (1/\Lambda, 0, \pm\sqrt{1 - 1/\Lambda^2}) \quad (\text{S12})$$

for $|\Lambda| < 1$. In addition, there is always a trivial fixed point at

$$\mathbf{S}/S = (1, 0, 0), \quad (\text{S13})$$

which is stable below the critical point and unstable above it.

Note that the definition of Λ must be modified to apply to the Floquet sequence in the main text. Since both the interaction and rotation per cycle are small, the effective Hamiltonian is equivalent to the static transverse field Ising model considered here, except with $\Lambda = \chi\tau_R/(h\tau_X)$. In this definition, τ_R and τ_X denote time for which we apply Ising interactions and rotations, respectively.

D. Effects of finite contrast

In the experiment, we measure the mean spin components normalized according to the total number of atoms N remaining at the end of the sequence: S_x/S , S_y/S and S_z/S , where $N = 2S$. We observe the mean normalized spin length $|\langle \mathbf{S} \rangle|/S = \mathcal{C}$ to be less than 1 and dependent on the number of Floquet cycles. The reduction of mean spin length affects the condition for the existence of the non-trivial fixed points, as any single normalized spin component cannot be larger than \mathcal{C} . From the prediction for the x -component of the fixed points $|S^x/S| = 1/\Lambda$, we arrive at a condition $|\Lambda| \geq 1/\mathcal{C}$. The coordinates of the fixed points are then also modified as $S_z = \sqrt{(\mathcal{C}S)^2 - S_x^2} = \mathcal{C}S\sqrt{1 - 1/(\mathcal{C}\Lambda)^2}$. Therefore the coordinates of the non-trivial fixed points are:

$$\mathbf{S}/(\mathcal{C}S) = (1/\Lambda_{\text{eff}}, 0, \pm\sqrt{1 - 1/(\Lambda_{\text{eff}})^2}), \quad (\text{S14})$$

where $\Lambda_{\text{eff}} = \mathcal{C}\Lambda$. This definition of Λ_{eff} implies that the ratio of independently measured χ and h must be scaled by the value of the reduced contrast \mathcal{C} to compare the mean-field model to experimental data.

-
- [1] J. Léonard, M. Lee, A. Morales, T. M. Karg, T. Esslinger, and T. Donner, New J. Phys. **16**, 093028 (2014).
 - [2] M. Foss-Feig, K. R. A. Hazzard, J. J. Bollinger, and A. M. Rey, Phys. Rev. A **87**, 042101 (2013).
 - [3] N. Šibalić, J. D. Pritchard, K. J. Weatherill, and C. S. Adams, Comput. Phys. Commun. **220**, 319 (2017).
 - [4] R. M. W. van Bijnen and T. Pohl, Phys. Rev. Lett. **114**, 243002 (2015).
 - [5] M. Kitagawa and M. Ueda, Phys. Rev. A **47**, 5138 (1993).